Ore Geology Reviews 63 (2014) 532–543

Contents lists available at ScienceDirect

Ore Geology Reviews

journal homepage: www.elsevier.com/locate/oregeorev

Fluorite REE-Y (REY) geochemistry of the ca. 850 Ma Tumen molybdenite–fluorite deposit, eastern Qinling, China: Constraints on ore genesis

Xiao-Hua Deng [a,b], Yan-Jing Chen [a,c,*], Jun-Ming Yao [c], Leon Bagas [d], Hao-Shu Tang [a,e]

[a] Key Laboratory of Orogen and Crust Evolution, Peking University, Beijing 100871, China
[b] Beijing Institute of Geology for Mineral Resources, Beijing 100012, China
[c] Key Laboratory of Mineralogy and Metallogeny, Guangzhou Institute of Geochemistry, Chinese Academy of Sciences, Guangzhou 510640, China
[d] Centre for Exploration Targeting, ARC Centre of Excellence for Core to Crust Fluid Systems, The University of Western Australia, Crawley, WA 6009, Australia
[e] State Key Laboratory of Ore Deposit Geochemistry, Institute of Geochemistry, Chinese Academy of Sciences, 46 Guanshui Road, Guiyang 550002, China

ARTICLE INFO

Article history:
Received 24 June 2013
Received in revised form 17 February 2014
Accepted 18 February 2014
Available online 25 February 2014

Keywords:
Fluorite
REY
Molybdenite–fluorite deposit
East Qinling Mo Belt
North China Craton

ABSTRACT

The Tumen molybdenite–fluorite vein system is hosted by carbonate rocks of the Neoproterozoic Luanchuan Group, located on the southern margin of the North China Craton (NCC) in central China. Previous studies divided the mineralization into four stages according to the crosscutting relationships between veinlets and their mineral assemblages. In this contribution, two distinctive types of fluorite mineralization are recognized: 1) the first type (Type 1) includes colourless, white or green fluorite grains present in Stage 1 veins; and 2) the second type includes Type 2a purple fluorite present in Stage 2 veins and does not coexist with sulfides, and Type 2b purple fluorite crystals associated with sulfides in Stage 2 veins. The rare earth element (REE) content in the fluorite ranges between 13.8 and 27.9 ppm in Type 1, 16.9 and 27.2 ppm in Type 2a, and 42.5 and 75.1 ppm in Type 2b, which suggests that the fluorite was precipitated from acidic fluids (given that REEs are mobile in saline HCl-bearing fluids at high temperature (~400 °C)). Comparing the REE chemistry of the Stage 1 against Stage 2 fluorite, the LREE/HREE ratios decrease from 9.8 to 4.0, La/Yb ratios decrease from 16.0 to 6.9 and La/Ho ratios decrease from 10.2 to 3.0, indicating that the hydrothermal process was at high-T and low-pH conditions. The Eu/Eu* ratios in the fluorite decrease from 1.11 ± 0.35 for Type 1 through 0.89 ± 0.19 for Type 2a to 0.75 ± 0.17 for Type 2b, suggesting a gradual increase in oxygen fugacity (fO_2) and pH of the mineralising fluid. The Tb/Ca, Tb/La and Y/Ho ratios of the fluorite types indicate that they were formed from the interaction between magmatic fluids and carbonate wallrocks. The fluorite samples show similar REE + Y (REY) patterns to those of dolostone units in the Luanchuan Group and the nearby Neoproterozoic syenite, suggesting that the REY in the fluorite was mainly sourced from the host-rocks, although the syenite could be an additional minor source.

1. Introduction

The eastward trending East Qinling Mo Belt (EQMB; Chen et al., 2000) extends along around the suture zone between the NCC and the Qinling Orogen (Fig. 1a, b). The belt is one of the most important Mo provinces in the world, which consists of six giant (>0.5 Mt) and many large (0.1–0.5 Mt), medium (0.01–0.1 Mt), and small (<0.01 Mt) deposits with a combined reserve of ~6 Mt Mo (Chen et al., 2009). The majority are Mesozoic porphyry- and skarn-type deposits formed in a post-subduction and collisional tectonic setting (Chen, 2013; Chen et al., 2000, 2007; Hu, 1988; Li et al., 2007, 2012a, 2012b, 2013; Mao et al., 2008). Most of the Mo deposits are located in the Huaxiong Block to the north of the Luanchuan Fault (Fig. 1b, c). The isotope ages obtained from these deposits range from Palaeoproterozoic to Early Cretaceous (Deng et al., 2013a, 2013b; Li et al., 2011b), suggesting that the Mo mineralisation in the EQMB can be traced back to 1.85 Ga.

Chen and Li (2009) suggested that the porphyry Mo systems in EQMB have high CO_2/H_2O and F/Cl ratios, and exhibit pronounced alteration characterised by K-feldspar, carbonate and fluorite, which are consistent observations made by other researchers (e.g. Pirajno, 2009, 2013; Y.F. Yang et al., 2013; Y. Yang et al., 2013; Yang et al., 2012). Why the Mo-mineralisation is usually related to fluoritization, however, is not well understood. Recently, Mo deposits have also been found in the carbonatite-, quartz- and fluorite-dominated veins in the Huaxiong Block (Chen et al., 2009; Deng et al., 2008, 2013c; Li et al.,

* Corresponding author at: Key Laboratory of Orogen and Crustal Evolution, Peking University, Beijing, 100871, China. Tel.: + 86 10 6275 7390.
E-mail addresses: yjchen@pku.edu.cn, gigyjchen@126.com (Y.-J. Chen).

http://dx.doi.org/10.1016/j.oregeorev.2014.02.009
0169-1368/

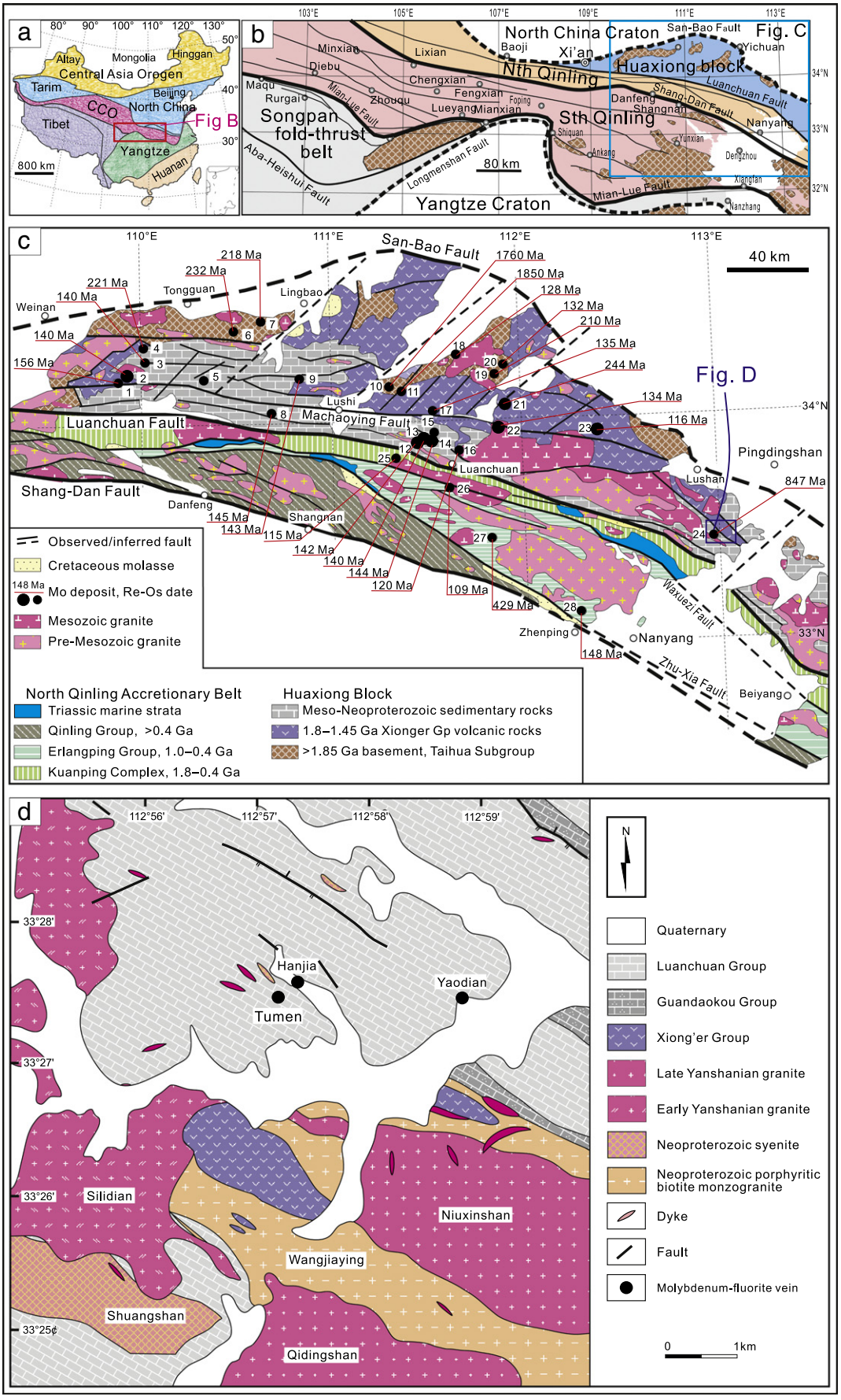
a
Altay
Mongolia
Hinggan
Central Asia Orogen
Tarim
Beijing
CCO
North China
Fig B
Tibet
Yangtze
Huanan
800 km
b
North China Craton
Fig. C
Baoji
Xi'an
Huaxiong block
Nth Qinling
Sth Qinling
Songpan fold-thrust belt
Yangtze Craton
80 km
c
San-Bao Fault
Fig. D
40 km
Luanchuan Fault
Shang-Dan Fault
Machaoying Fault
Waxuezi Fault
Zhu-Xia Fault
Observed/inferred fault
Cretaceous molasse
Mo deposit, Re-Os date
Mesozoic granite
Pre-Mesozoic granite
North Qinling Accretionary Belt
Triassic marine strata
Qinling Group, >0.4 Ga
Erlangping Group, 1.0–0.4 Ga
Kuanping Complex, 1.8–0.4 Ga
Huaxiong Block
Meso-Neoproterozoic sedimentary rocks
1.8–1.45 Ga Xionger Gp volcanic rocks
>1.85 Ga basement, Taihua Subgroup
d
Hanjia
Tumen
Yaodian
Silidian
Niuxinshan
Wangjiaying
Shuangshan
Qidingshan
Quaternary
Luanchuan Group
Guandaokou Group
Xiong'er Group
Late Yanshanian granite
Early Yanshanian granite
Neoproterozoic syenite
Neoproterozoic porphyritic biotite monzogranite
Dyke
Fault
Molybdenum-fluorite vein
0 1km

2011a; Pirajno, 2013; Xu et al., 2010). The discovery of the unique Tumen Mo–F deposit in the terrane provides a good example to investigate the genetic relationship between fluorine and molybdenum in the Qinling Orogen.

The REE and trace element characteristics of a hydrothermal fluid are primarily controlled by physio-chemical conditions during fluid–rock interactions and fluid migration (Bau and Möller, 1992; Schwinn and Markl, 2005). Their concentrations in minerals have become a powerful tool in studying the genesis of hydrothermal ore (e.g. Bau and Dulski, 1995; Eppinger and Closs, 1990; Möller and Holzbecher, 1998; Zhao, 1997), and environmental changes (e.g. Bau and Dulski, 1996; Chen and Fu, 1991; Chen and Zhao, 1997; Tang et al., 2009, 2013).

REE geochemistry has been extensively used to study the genesis of fluorite concentrations in different geological environments (e.g. Bau et al., 2003; Möller et al., 1976; Schwinn and Markl, 2005). Fluorite is not only an economically important mineral, but also an important gangue mineral associated with Pb–Zn, Ag, Mo, W and Sn deposits (e.g. Chen and Li, 2009; Eppinger and Closs, 1990; Hill et al., 2000). Therefore, the study of REE concentration in fluorite of different hydrothermal stages can provide insights into the evolution of a fluid through time, the fluid–rock interaction and element behaviour in ore-forming processes, and can be widely used as a geochemical exploration tool (e.g. Bau and Möller, 1992; Cao, 1997; Goff et al., 2004; Jiang et al., 2006; Möller, 2001; Ronchi et al., 1993; Sánchez et al., 2010; Schönenberger et al., 2008; Subías and Fernández-Nieto, 1995).

In this contribution, we document a significant variation in trace element contents in different kinds of fluorite at the Tumen Mo–F deposit and, thereby, explore the importance of hydrothermal processes related to the genesis and association of Mo and F mineralisation.

2. Regional geology

The Qinling Orogen is in the central portion of the east-trending Central China Orogen (CCO), which evolved when the northernmost Palaeo-Tethys Ocean finally closed during the Mesozoic collision between the NCC and the Yangtze Craton (Fig. 1a; Pirajno, 2013; Ratschbacher et al., 2003). The Orogen is bounded to the north by the San–Bao Fault and to the south by the Longmenshan–Dabashan Fault.

Four tectonic units have been recognized in the Orogen by Chen et al. (2009) and Dong et al. (2011). These subdivisions from north to south are: (1) the Huaxiong Block that represents the activated southern margin of the NCC; (2) the northern Qinling accretionary belt; (3) the southern Qinling orogenic belt; and (4) the northern margin of the Yangtze Craton. The Luanchuan Fault separates the Huaxiong Block and the northern Qinling accretionary belt, the Shang-Dan Fault separates the northern Qinling accretionary and southern Qinling orogenic belts, and the Mian-Lue Fault separates the southern Qinling orogenic belt from the Yangtze Craton to the south (Fig. 1b).

Molybdenite–fluorite mineralisation is located in the southeastern part of the Huaxiong Block, which is bounded by the San–Bao Fault to the north and the Luanchuan Fault to the south (Fig. 1c; Deng et al., 2013c). This region consists of an early Palaeoproterozoic (2.3–2.15 Ga) crystalline basement named the Taihua Supergroup, which is unconformably overlain by the Palaeoproterozoic Xiong'er Group and Meso–Neoproterozoic sedimentary rocks assigned to the Guandaokou and Luanchuan groups (Chen and Fu, 1992; Chen and Zhao, 1997).

The Taihua Supergroup consists of sillimanite–garnet–quartz gneiss, graphite-bearing gneiss, marble, and banded iron formations. The supergroup is interpreted as a greenstone succession metamorphosed at the amphibolite to granulite facies (Chen and Zhao, 1997; Xu et al., 2009). The metamorphism took place around ca. 1.95–1.82 Ga during the assembly of the Columbia Supercontinent; also known as the Nuna or Hudsonland Supercontinent (Santosh, 2010; Santosh et al., 2007a, 2007b; Wan et al., 2006; Zhai and Santosh, 2011; Zhao et al., 2004, 2009).

The Xiong'er Group is a well-preserved non-metamorphosed volcanic sequence consisting predominantly of basaltic andesite and andesite, with minor amounts of dacite and rhyolite (He et al., 2009). The group is subdivided into the Dagushi Formation at the base through the Xushan and Jidanping formations to the Majiahe Formation at the top (Zhao et al., 2009). Available SHRIMP and LA-ICP-MS U–Pb zircon age data suggest that the volcanic rocks erupted intermittently over a protracted interval between 1.84 and 1.45 Ga with a major phase of volcanism during 1.78–1.75 Ga (Hu, 1988; Zhao et al., 2009). The origin of the group is still being debated, with some authors suggesting it developed in a continental-rift environment (e.g. Sun et al., 1985; T.P. Zhao et al., 2002), as part of a large igneous province linked to a mantle plume (e.g. Peng et al., 2008), or as an Andean-type continental-arc tectonic setting (e.g. Chen and Fu, 1992; G.C. Zhao et al., 2002; He et al., 2009; Zhao et al., 2004, 2009).

The Guandaokou and Luanchuan groups consist of a variably carbonaceous succession of carbonate, shale, and chert. These units have been deposited along the southern margin of the Huaxiong Block (Fig. 1c; Jiang et al., 1994; Wang et al., 2011).

The Tumen deposit is hosted by dolostone assigned to the Meso–Neoproterozoic Luanchuan Group, and is located in the southeast part of the Huaxiong Block (Fig. 1d), where volcanic rocks of the Xiong'er Group are overlain by clastic and carbonate rocks of the Guandaokou and Luanchuan groups (Jiang et al., 1994). The Neoproterozoic Wangjiaying Granite (consisting of a porphyritic biotite monzogranite), and the ca. 844 Ma Shuangshan Syenite represent Neoproterozoic magmatism in the region (Bao et al., 2008). The Precambrian rock units discussed above are intruded by Yanshanian (180–98 Ma) granites, including the Silidian, Niuxinshan and Qidingshan granites (Fig. 1d).

3. Ore geology and fluid inclusions

The Tumen deposit includes numerous molybdenite–fluorite veins clustering in the Tumen, Hanjia and Yaodian areas (Fig. 1d). These 1 to 10 m thick veins are mainly hosted by dolostone and schist in the Neoproterozoic Luanchuan Group, and can be traced for several kilometres along a NW-trending fault zone (Fig. 2a). The veins contain 60–94% fluorite and were initially mined to depths of <250 m (Fig. 2b), with a minimum fluorite reserve of 2 Mt (Wen, 1997). During the mining process, it was found that the molybdenite content in the fluorite veins increased in depth with grades reaching 10% Mo. In general, the economic reserves of Mo are at a depth >150 m, with average grades ranging from 0.05 to 3% Mo. The molybdenite–fluorite veins at the Tumen area inferred to contain a minimum resource of 0.01 Mt Mo in metal (Ye et al., 2004).

Four Mo-mineralised veins have been identified at Tumen that are locally called the Nos. 5–2, 5–3, 5–4 and 6 orebodies (Fig. 2), which are lenticular to tabular in shape (Fig. 2a), spatially controlled by NW-trending faults and are associated with syenite dykes (Fig. 2b). The mineralisation is stratigraphically controlled in a transition zone between quartz–sericite schist and dolomite. The mineralisation in the orebodies is dominated by molybdenite and pyrite with lesser amounts of sphalerite, galena and chalcopyrite. Gangue minerals are typically fluorite, calcite and quartz, with minor amounts of muscovite and sericite. Hydrothermal alteration is characterised by a combination

Fig. 1. Maps showing: (a) the major tectonic subdivisions of China, showing the location of the Qinling Orogen; (b) tectonic framework of the Qinling Orogen; (c) distribution of Mo deposits in the East Qinling Mo Belt; and (d) the regional geology of the Tumen Mo–F deposit (modified from Chen et al., 2009 and references therein; Deng et al., 2013c). Names of numbered deposits: 1—Balipo; 2—Jinduicheng; 3—Shijiawan; 4—Huanglongpu; 5—Mulonggou; 6—Majiawa; 7—Dahu; 8—Yechangping; 9—Yinjiagou; 10—Zhaiwa; 11—Longmendian; 12—Shangfanggou; 13—Nannihu; 14—Sandaozhuang; 15—Majuan; 16—Zhuyuangou; 17—Shiyaogou; 18—Shapoling; 19—Huangshui'an; 20—Leimengou; 21—Waifangshan Mo ore district; 22—Yuchiling; 23—Donggou; 24—Tumen; 25—Saozhoupo; 26—Shimengou; 27—Yindonggou; 28—Qiushuwan. Abbreviation CCO: Central China Orogen (includes the Kunlun, Qilian, Qinling, and Dabie orogenic belts).

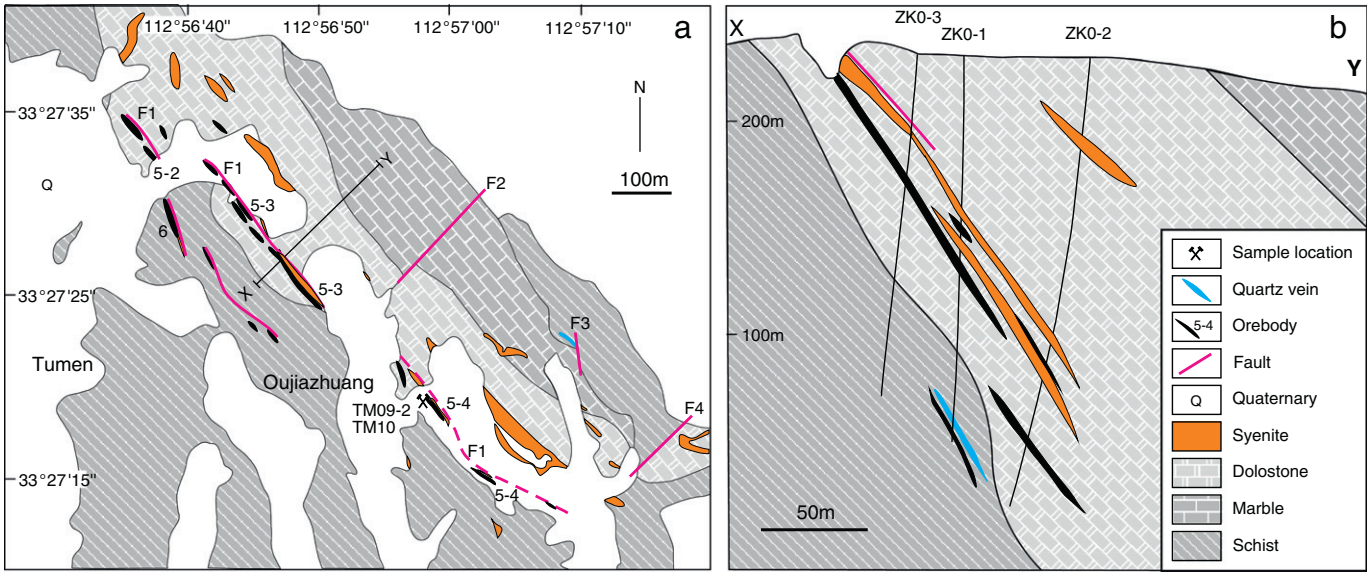

Fig. 2. Geological map (a) and cross-section (b) of the Tumen Mo–F deposit (after Deng et al., 2013c).

of silica, fluorite, carbonate, and kaolinite. Based on the mineral assemblages observed and crosscutting relationships of the veins, the mineralisation can be divided into four stages (Deng et al., 2013c). Stage 1 is represented by brecciated white to green fluorite veins, Stage 2 by veins of purple fluorite (–molybdenite–pyrite), Stage 3 by the assemblage calcite–pyrite(–sphalerite–chalcopyrite), and Stage 4 by sulfide-barren carbonate veins.

Three types of fluid inclusions have been recognized in the fluorite crystals associated with the ore according to their composition and phase-types (Deng et al., 2013c). Specifically, these are aqueous, CO_2-bearing, and daughter mineral-bearing inclusions. It appears that the fluorite crystals formed at different stages contain distinct fluid inclusion assemblages. In Stage 1 white fluorite, assemblages recognized consisting of: (1) aqueous-only inclusions; and (2) aqueous, CO_2-bearing and daughter mineral-bearing inclusions. Stage 2 purple fluorite contains: (1) aqueous-only inclusions; (2) both aqueous and CO_2-bearing inclusions; and (3) both CO_2-bearing and daughter mineral-bearing inclusions. Only aqueous inclusions have been observed in Stages 3 and 4 calcite.

The homogenization temperatures of fluid inclusions in Stage 1 fluorite ranges from 420° to 360 °C and in Stage 2 fluorite between 300 °C and 220 °C. Similarly, salinities of the fluid inclusions decrease from 39.8 wt.% NaCl equiv. in Stage 1 fluorite, to 0.4–13.1 wt.% NaCl equiv. in Stage 2 fluorite. This shows that the ore-forming system evolved from an early high-salinity at high-temperature H_2O–CO_2–NaCl fluid (Stage 1), to a late dilute, CO_2-poor and moderate temperature H_2O–NaCl fluid (Stage 2). Furthermore, the trapping pressure of Stage 2 CO_2-bearing inclusions was estimated at 185–282 MPa, suggesting that the mineralisation depth ranges from 6.2 to 9.4 km under lithostatic pressure (Deng et al., 2013c).

Seven molybdenite analyses from the molybdenite–fluorite veins yield Re–Os isotope ages ranging from 846 ± 7 Ma to 965 ± 7 Ma, with an isochron age of 847 ± 7 Ma (2σ, MSWD = 23), suggesting that the molybdenite–fluorite mineralisation formed at ca. 850 Ma (Deng et al., 2013c). This Re–Os isochron age is the same within error as the LA-ICP-MS zircon U–Pb age of 844 ± 2 Ma for the Shuangshan Syenite near Tumen (Bao et al., 2008), but is slightly older than the SHRIMP and LA-ICP-MS zircon U–Pb ages of ca. 830 Ma for gabbro dated within the Huaxiong Block (Wang et al., 2011). This older date suggests that the genesis of the Tumen Mo–F mineral system was related to the beginning Neoproterozoic rifting at the southern margin of the NCC slightly prior to the emplacement of the gabbro.

4. Samples and analytical methods

4.1. Sample distinction

Sixteen representative samples of fluorite from the Tumen deposit were assayed for trace elements. The types of the fluorite are identified by their mineral associations and the crosscutting relationships of the mineralised veins (Fig. 3). The Type 1 fluorite samples (TM-14, TM-15, TM-18-1 and TM-19), hosted by Stage 1 veins, are typically white or colourless, subhedral to anhedral, and 0.2–6 mm in diameter. Type 2a fluorite samples (TM-03, TM-05, TM-08, TM-11, TM-12, TM-13, TM-18-2 and TM-2) are hosted by Stage 2 veins and are purple, anhedral, are not associated with sulfides, and are 0.05–8 mm in diameter. Stage 2 veins host Type 2b fluorites (Samples TM-06, TM-07, TM-09 and TM-10), which are purple in colour and commonly associated with pyrite and molybdenite.

4.2. Analytical methods

Fluorite grains were handpicked under a binocular microscope (purity >99%), and then milled to a 200 mesh for trace element analyses using an inductively coupled plasma mass spectrometry (ICP-MS) with a Finnegan MAT Element spectrometer; The analytical uncertainties are within 5% for most elements reported. The analyses were done at the Institute of Geology and Geophysics, Chinese Academy of Sciences in Beijing (Jin and Zhu, 2000).

Powders (40 mg) were dissolved in distilled HF + HNO_3 in high pressure sealed Teflon bombs at 200 °C for 5 days, dried, and then digested with HNO_3 at 150 °C for 1 day, and the final step was repeated. Dissolved samples were diluted to 50 ml with 1% HNO_3 and 1 ml 500 ppb indium was added to the solution as an internal standard. A blank solution was analysed and the total procedural blank was <50 ng for all trace elements. Indium was used as an internal standard to correct for matrix effects and instrument drift. Precision for all trace elements is estimated to be 5% and accuracy is better than 5% for most elements by analyses of the GSR-3 standard (Table 1).

5. Results

The analytical results are listed in Table 1. Strontium and barium can be incorporated as cations into fluorite due to their similar size and charge to Ca. The Type 1 fluorite assays between 658 and 1117 ppm

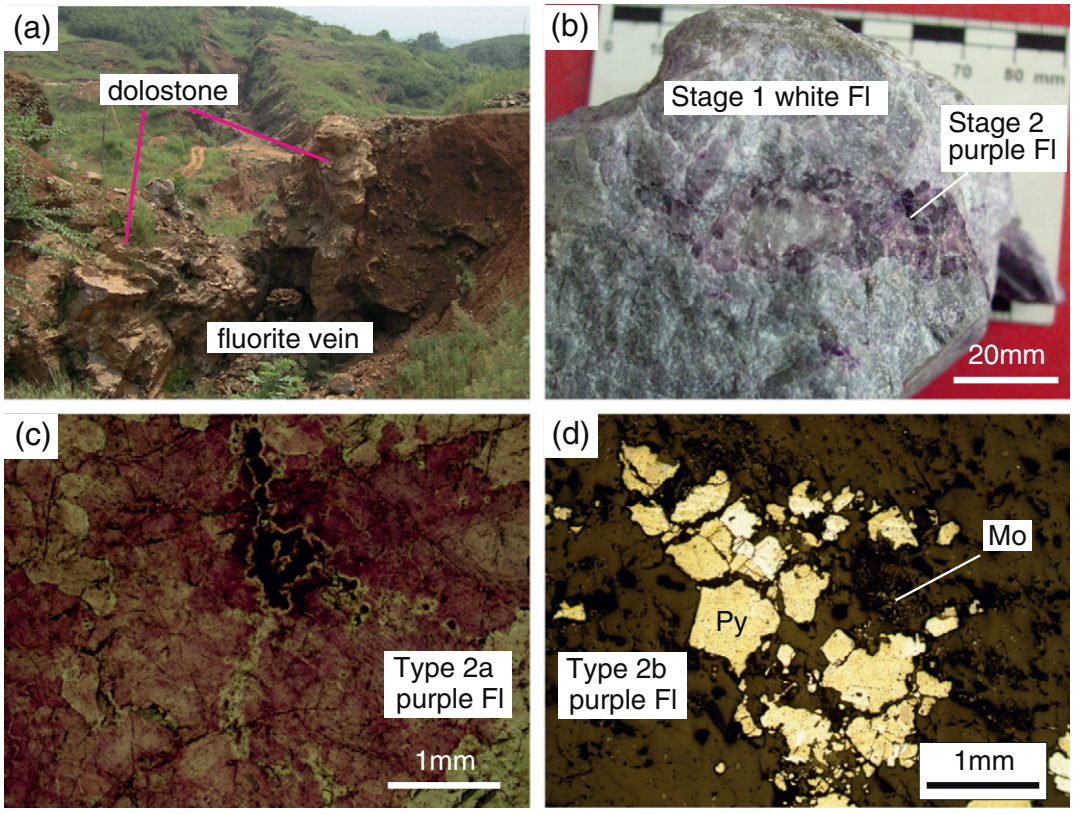

Fig. 3. Photographs of: (a) near vertical fluorite vein cutting a dolostone bed in the Luanchuan Group; (b) Stage 1 white fluorite (Type 1) vein cut by the Stage 2 purple fluorite vein; (c) Stage 2 purple fluorite without coexisting sulfides (Type 2a); and (d) photomicrograph showing the intergrowth of Type 2b purple fluorite with pyrite and molybdenite.

Sr and 32.5–697 ppm Ba, Type 2a fluorite assays between 882 and 1564 ppm Sr and 40.2–2789 ppm Ba, and Type 2b ranges between 331 and 1292 ppm Sr and 61.6–980 ppm Ba.

Type 1 fluorite has a much lower U content (0.06–1.75 ppm) than those of Types 2a and 2b (0.28–97.6 ppm; Table 1, Fig. 4), resembling the variations of REE in fluorites from the deposit (discussed below). This possibly resulted from the REE-U isomorphic substitution or co-precipitation from the solution, due to their similarity in ion radii (Dai, 1987).

Fluorite grains from the different mineralisation stages show different REE geochemical characteristics (Table 1). Total REE concentrations (ΣREE) in Type 1 fluorites assay 13.8–27.9 ppm (averaging 20.7 ± 6.0 ppm ΣREE), Type 2a assay 16.9–27.2 ppm (averaging 23.0 ± 4.0 ppm ΣREE), and Type 2b assay 42.5–75.1 ppm (55.2 ± 14.0 ppm ΣREE) (Table 1). From this data, it is clear that Stage 2a fluorite has slightly higher ΣREE values than Stage 1 fluorite, whereas Stage 2b fluorite (which is associated with sulfides) has the highest ΣREE values. The Y contents in the types of fluorite have an overall increasing trend, with assays of 2.29–9.23 ppm Y for Type 1, 10.5–23.6 ppm Y for Type 2a, and 13.6–26.2 ppm Y for Type 2b. The contents and various trends of REE and Y of the three types of fluorite are different, indicating that the REE and Y might have been fractionated in a fluorine-rich aqueous fluid due to Y acting as a pseudolanthanide that is heavier than Lu. This fractionation is not a source-related phenomenon, but depends on fluid composition (Bau and Dulski, 1995).

The chondrite-normalized REE + Y (REY) diagrams for the fluorite samples are weakly enriched in LREE (Fig. 5), and Type 2a fluorite REY patterns are more flatten than those of Types 1 and 2b. The $(La/Ho)_N$ average for Type 2a (3.0 ± 1.0) fluorite is also lower than for Type 1 (10.2 ± 4.8) and Type 2b (8.1 ± 2.8). The $(La/Yb)_N$ ratios for the three types have similar trends to those of the $(La/Ho)_N$ averages (Table 1).

All of the fluorite samples show striking positive Y anomalies with mean ratios of 1.59 ± 0.46 for Type 1, 1.92 ± 0.35 for Type 2a, and 2.18 ± 0.45 for Type 2b. The samples do not have obvious Ce anomalies, but the Ce/Ce* ($Ce/Ce^* = Ce_N/[(La_N + Pr_N)/2]$) values decrease from 0.90–1.03 for Type 1, through 0.82–0.92 for Type 2a, to 0.79–0.88 for Type 2b fluorites. The Eu/Eu* ($Eu/Eu^* = Eu_N/[(Sm_N + Gd_N)/2]$) ratios also decrease from Type 1 (0.88–1.62), through Type 2a (0.68–1.20), to Type 2b (0.65–1) fluorites.

6. Discussion

6.1. Variation in ΣREE

It is known that the ΣREE concentration in hydrothermal fluids is controlled by the pH and bulk chemical composition of solutions (e.g. Schwinn and Markl, 2005). Michard (1989) showed that the REE concentrations in fluids increase along with decreasing pH. As outlined above, the average ΣREE content of Types 1, 2a and 2b fluorite samples are 20.7 ± 6, 23 ± 4 and 55.2 ± 14 ppm, respectively (i.e. increasing from Stage 1 to Stage 2; Table 1). Deng et al. (2013c) observed that the salinity of fluids in the Stage 1 mineralisation was much higher than that in Stage 2, and conversely the CO_2 content increases from Stage 1 to Stage 2. These characteristics imply that the differences in ΣREE in fluorite in the different types were possibly related to changes in pH or variation in the composition of the mineralising fluid from Stage 1 to Stage 2.

We can infer from the low ΣREE values for Stage 1 fluorite that the initial fluids were acidic and rich in both HF and F. Such a fluid can keep REE cations (R^{3+}) in solution and possibly as R^{3+}–F^- complexes (e.g. Bau and Dulski, 1995; Gramaccioli et al., 1999). This is consistent with the assumptions: (1) the fluids forming fluorite veins were rich in F^-, which must be maintained by high H^+ activity due to the reaction $HF + F^- \Leftrightarrow H^+ + 2\,F^-$ (Dai, 1987); (2) the shortage of sulfides in Stage 1 veins indicates that the fluid was acidic and the S^{2-} activity low, thus preventing sulfide precipitation from the solution,

Table 1
Concentrations of rare earth and trace elements in fluorite of various types from the Tumen deposit (ppm).

Type	1	1	1	1		2a	2a	2a	2a	2a	2a	2a	2a		2b	2b	2b	2b		GSR3	GSR3
No.	TM-14	TM-15	TM-18-1	TM-19	Av.	TM-03	TM-05	TM-08	TM-11	TM-12	TM-13	TM-18-2	TM-20	Av.	TM-06	TM-07	TM-09	TM-10	Av.	RVR	Av.
Li	0.11	0.48	0.11	0.06	0.19	0.83	0.53	0.32	0.95	0.86	0.35	0.37	0.72	0.62	0.45	4.38	0.24	2.14	1.80	9.50	9.13
Be	0.16	0.54	0.15	0.14	0.25	0.73	0.42	0.42	0.29	0.24	0.35	0.31	0.39	0.39	0.65	1.18	0.16	1.03	0.75	2.50	2.56
Sc	0.68	1.40	1.25	1.65	1.24	0.37	0.19	0.25	1.17	0.36	0.37	1.30	0.96	0.62	0.56	1.70	1.18	1.39	1.21	15.2	14.4
V	28.2	25.0	22.7	23.0	24.7	26.7	27.9	31.8	28.4	18.2	21.9	29.2	23.0	25.9	24.0	36.1	27.2	28.4	28.9	167	171
Cr	7.09	3.82	4.11	2.52	4.38	4.94	4.86	6.78	3.55	4.40	4.35	6.24	4.10	4.90	3.03	13.4	4.37	4.60	6.35	134	146
Co	0.69	1.93	0.64	0.69	0.99	0.73	1.15	0.92	1.91	4.38	4.84	0.84	0.79	1.94	7.03	12.3	2.23	2.45	6.01	46.5	45.6
Ni	8.49	7.87	7.99	4.23	7.14	4.77	6.27	7.43	10.6	10.5	18.6	6.10	6.29	8.82	19.2	18.8	8.91	9.92	14.2	140	132
Cu	0.34	16.0	0.13	0.65	4.29	1.72	2.34	0.89	1.19	2.01	7.02	0.77	3.64	2.45	6.48	3.31	0.90	2.37	3.26	48.6	46.7
Zn	18.0	120	8.94	37.5	46.2	22.0	11.1	61.7	96.0	28.7	14.3	23.6	1378	204	38.3	466	17.7	53.7	144	150	148
Ga	0.31	1.05	0.26	0.13	0.44	2.40	2.09	0.79	1.38	0.71	0.50	0.89	1.03	1.22	0.91	4.67	0.84	3.28	2.43	24.8	23.7
Rb	0.87	3.08	0.54	0.26	1.18	14.3	13.6	3.39	9.13	5.72	3.13	5.16	6.74	7.64	4.50	32.0	4.26	12.4	13.3	37.0	35.7
Sr	944	658	930	1117	912	1231	1319	1564	1067	914	1107	1014	882	1137	1292	331	772	634	757	1100	1007
Y	3.70	9.23	4.27	2.29	4.87	10.5	15.6	11.4	13.7	15.2	11.2	13.2	23.6	14.3	13.6	26.2	25.8	25.5	22.8	22.0	21.2
Zr	3.95	16.4	2.82	2.75	6.49	7.01	8.88	5.31	4.98	3.99	6.89	8.03	10.6	6.97	8.12	24.2	46.4	12.9	22.9	277	268
Nb	0.56	2.00	0.51	0.47	0.88	1.33	1.58	1.04	1.14	1.54	3.52	1.57	1.72	1.68	6.29	15.1	2.12	3.39	6.72	68.0	66.7
Cs	0.03	0.06	0.03	0.02	0.03	0.10	0.08	0.05	0.11	0.08	0.05	0.05	0.07	0.07	0.06	0.48	0.03	0.24	0.20	0.49	0.45
Ba	32.5	278	49.6	697	264	2789	1615	463	544	92.3	40.2	141	161	731	61.6	980	260	92.5	348	526	497
La	3.56	6.32	3.69	3.34	4.23	3.66	4.28	2.48	3.75	4.12	3.23	3.22	2.96	3.46	11.3	15.5	11.3	15.1	13.3	56.0	54.6
Ce	7.91	11.7	9.57	6.30	8.87	7.79	8.13	5.35	7.71	8.30	6.09	8.13	6.47	7.25	18.1	27.8	19.5	21.5	21.7	105	98.3
Pr	0.95	1.38	1.29	0.72	1.09	1.16	1.11	0.88	1.26	1.36	0.87	1.32	1.01	1.12	1.95	3.73	2.13	2.19	2.50	13.2	12.7
Nd	3.06	4.67	4.60	2.01	3.58	4.60	4.62	3.64	5.31	5.61	3.19	5.99	4.82	4.72	6.12	14.5	7.53	6.75	8.72	54.0	52.4
Sm	0.60	0.79	0.92	0.33	0.66	1.01	1.03	0.83	1.16	1.27	0.65	1.55	1.56	1.13	0.96	2.81	1.56	1.09	1.60	10.2	9.83
Eu	0.18	0.26	0.29	0.18	0.23	0.28	0.33	0.26	0.34	0.32	0.16	0.67	0.70	0.38	0.22	0.67	0.59	0.28	0.44	3.20	3.07
Gd	0.63	0.92	0.80	0.36	0.68	1.18	1.26	1.02	1.31	1.65	0.81	1.88	2.35	1.43	1.09	3.03	2.09	1.55	1.94	8.50	7.99
Tb	0.10	0.15	0.13	0.05	0.11	0.19	0.22	0.17	0.22	0.26	0.14	0.32	0.45	0.24	0.18	0.50	0.36	0.27	0.33	1.20	1.12
Dy	0.62	0.85	0.69	0.26	0.61	1.10	1.36	1.08	1.31	1.51	0.88	2.02	2.87	1.52	1.17	3.01	2.35	1.75	2.07	5.60	5.35
Ho	0.11	0.16	0.13	0.05	0.11	0.21	0.28	0.21	0.26	0.28	0.18	0.38	0.58	0.30	0.24	0.59	0.49	0.36	0.42	0.88	0.88
Er	0.28	0.39	0.30	0.12	0.27	0.51	0.71	0.53	0.61	0.70	0.47	0.93	1.51	0.75	0.60	1.50	1.27	0.93	1.08	2.00	1.90
Tm	0.04	0.05	0.04	0.02	0.03	0.06	0.09	0.07	0.07	0.08	0.06	0.12	0.20	0.09	0.08	0.20	0.17	0.12	0.14	0.28	0.24
Yb	0.22	0.26	0.22	0.09	0.20	0.36	0.49	0.35	0.39	0.43	0.34	0.62	1.09	0.51	0.44	1.10	0.97	0.66	0.79	1.50	1.30
Lu	0.03	0.04	0.03	0.01	0.03	0.05	0.06	0.05	0.05	0.06	0.05	0.08	0.13	0.07	0.06	0.14	0.12	0.08	0.10	0.19	0.17
Hf	0.13	0.30	0.11	0.11	0.16	0.15	0.19	0.14	0.13	0.11	0.15	0.19	0.25	0.16	0.16	0.55	0.44	0.22	0.34	6.50	6.28
Ta	0.05	0.08	0.05	0.05	0.06	0.06	0.08	0.05	0.05	0.05	0.05	0.08	0.08	0.06	0.06	0.14	0.08	0.07	0.09	4.30	4.17
Tl	0.05	0.07	0.04	0.04	0.05	0.20	0.19	0.09	0.20	0.25	0.12	0.15	0.12	0.16	0.17	0.57	0.27	0.19	0.30	0.12	0.06
Pb	5.05	5.33	1.92	9.71	5.50	23.2	4.49	70.9	134	19.4	7.94	6.60	6.73	34.2	14.6	10.8	16.1	12.5	13.5	4.70	4.83
Bi	0.02	0.02	0.01	0.02	0.02	0.03	0.02	0.06	0.28	0.02	0.02	0.02	0.02	0.06	0.02	0.03	0.02	0.02	0.02	0.05	0.04
Th	0.15	0.47	0.13	0.12	0.22	0.31	0.60	0.13	0.29	0.14	0.24	0.39	0.48	0.32	0.37	1.75	1.06	0.63	0.95	6.00	6.32
U	0.13	1.75	0.08	0.06	0.50	4.45	2.71	23.4	49.3	97.6	18.9	0.28	0.83	24.7	34.5	173	3.35	78.9	72.6	1.40	1.42
ΣREE	18.3	27.9	22.7	13.8	20.7 ± 6.0	22.2	24.0	16.9	23.7	25.9	17.1	27.2	26.7	23.0 ± 4.0	42.5	75.1	50.5	52.7	55.2 ± 14.0		
LREE	16.3	25.1	20.3	12.9	18.7 ± 5.3	18.5	19.5	13.4	19.5	21.0	14.2	20.9	17.5	18.1 ± 2.9	38.7	65.0	42.7	46.9	48.3 ± 11.6		
HREE	2.04	2.82	2.34	0.95	2.0 ± 0.8	3.66	4.46	3.48	4.22	4.96	2.93	6.35	9.18	4.9 ± 2.0	3.85	10.08	7.82	5.73	6.9 ± 2.7		
LREE/HREE	7.99	8.91	8.69	13.5	9.8 ± 2.5	5.06	4.38	3.86	4.63	4.23	4.85	3.29	1.91	4.0 ± 1.0	10.1	6.44	5.46	8.20	7.5 ± 2.0		
$(La/Yb)_N$	10.9	16.4	11.3	25.6	16.0 ± 6.9	6.95	5.95	4.74	6.50	6.51	6.51	3.52	1.83	5.3 ± 1.8	17.4	9.53	7.94	15.4	12.6 ± 4.6		
$(La/Ho)_N$	7.37	9.27	6.84	17.2	10.2 ± 4.8	4.01	3.60	2.69	3.40	3.38	4.11	1.96	1.18	3.0 ± 1.0	11.0	6.09	5.41	9.78	8.1 ± 2.8		
La/Ho	31.8	40.0	29.5	74.1	43.9 ± 20.7	17.3	15.5	11.6	14.7	14.6	17.7	8.46	5.10	13.1 ± 4.4	47.6	26.3	23.3	42.2	34.9 ± 11.9		
Y/Ho	33.0	58.4	34.1	50.9	44.1 ± 12.6	49.6	56.4	53.6	53.6	53.9	61.4	34.7	40.6	50.5 ± 8.7	57.2	44.4	52.9	71.0	56.4 ± 11.1		
$(La/Nd)_N$	2.26	2.62	1.55	3.22	2.4 ± 0.7	1.54	1.80	1.32	1.37	1.42	1.96	1.04	1.19	1.5 ± 0.3	3.58	2.08	2.92	4.35	3.2 ± 1.0		
$(Gd/Yb)_N$	2.31	2.86	2.95	3.32	2.9 ± 0.4	2.69	2.09	2.33	2.71	3.13	1.96	2.47	1.74	2.4 ± 0.5	2.01	2.24	1.75	1.89	2.0 ± 0.2		
Eu/Eu*	0.88	0.92	1.00	1.62	1.11 ± 0.35	0.79	0.89	0.87	0.84	0.68	0.69	1.20	1.12	0.89 ± 0.19	0.66	0.70	1.00	0.65	0.75 ± 0.17		
Ce/Ce*	0.99	0.90	1.03	0.92	0.96 ± 0.06	0.88	0.86	0.85	0.83	0.82	0.84	0.92	0.88	0.86 ± 0.03	0.84	0.84	0.88	0.79	0.84 ± 0.04		
Y/Y*	1.20	2.15	1.24	1.79	1.59 ± 0.46	1.87	2.17	2.04	2.02	1.99	2.40	1.29	1.56	1.92 ± 0.35	2.21	1.68	2.06	2.76	2.18 ± 0.45		

Abbreviations: GSR3, Chinese basalt standard; RVR, recommended value for reference standard; Av., average. $Eu/Eu^* = Eu_N/[(Sm_N + Gd_N)/2]$, $Ce/Ce^* = Ce_N/[(La_N + Pr_N)/2]$, $Y/Y^* = Y_N/[(Dy_N + Ho_N)/2]$.

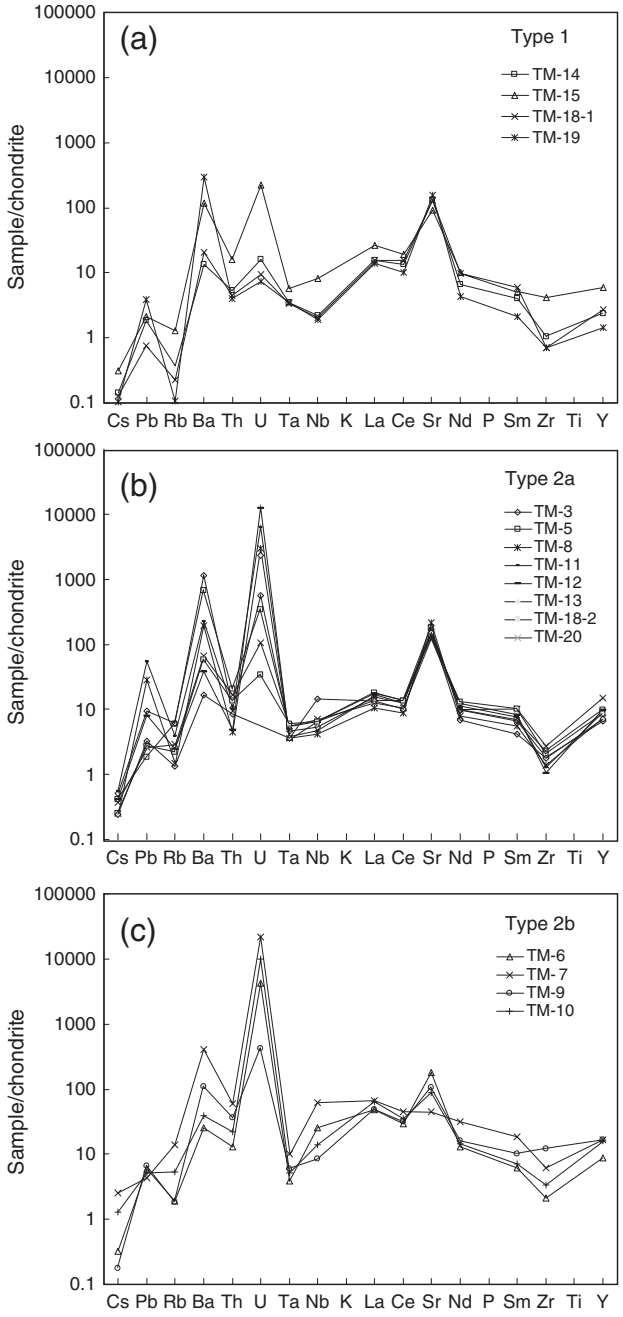

Fig. 4. The chondrite-normalized trace element patterns for fluorite samples from the Tumen Mo–F deposit. The reference data of chondrite are cited from McDonough and Sun (1995).

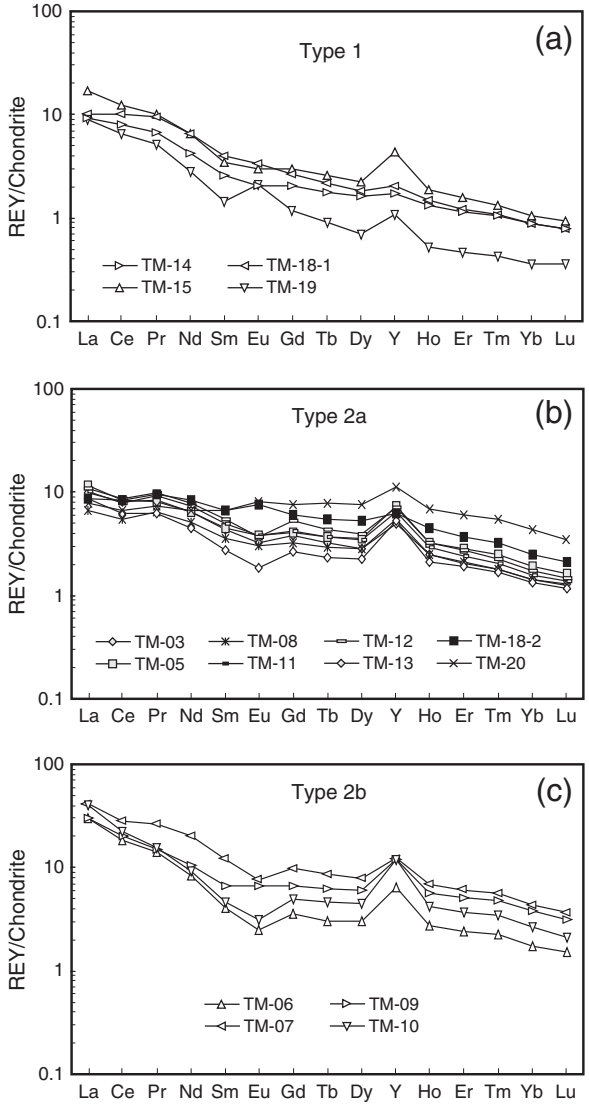

Fig. 5. Chondrite-normalized REY (REE-Y) patterns for fluorite samples from the Tumen Mo–F deposit. The reference data of chondrite are cited from Taylor and McLennan (1985).

(i.e. according to the reaction $H^+ + S^{2-} \Leftrightarrow HS^-$; Phillips and Evans, 2004); (3) the presence of S^{2-} or HS^- resulted in a reducing environment in which R^{3+} tended to remain in the fluid, with the exception of Eu^{3+} that was likely reduced to Eu^{2+}, and consequently the fluorite is characterized by a low ΣREE content and a high Eu/Eu* ratio (see Chen and Zhao, 1997 for the chemical principles involved); and (4) the interaction of the acidic and F^--rich fluids with the carbonate wallrocks resulted in the dissolution of $CaCO_3$ and formation of CaF_2 according to the reaction $CaCO_3 + 2H^+ + 2\,F^- \Leftrightarrow CaF_2 + H_2O + CO_2$, resulting in an increase in the CO_2 content of the Stage 2 fluid (Deng et al., 2013c).

Fluorite deposition in Stage 1 resulted in the reduction of the acidity of the fluid, and conversely the drop in pH lead to reduction of the solubility of R^{3+}. This subsequently enhanced the activity of S^{2-} in Stage 2 fluid leading to the deposition of REE and sulfides such as MoS_2 and FeS_2 (i.e. $Mo^{4+} + 2S^{2-} \Leftrightarrow MoS_2$). The Stage 2 purple fluorite, therefore, will have higher REE concentrations irrespective of whether it coexists with sulfides (Type 2b) or not (Type 2a). It is envisaged that the physicochemical nature of the fluid was not homogeneous along the ore-hosting faults. Local accumulation of S^{2-}, possibly together with HS^-, resulted in or from locally high-pH levels, where they were favourable for the deposition of sulfides and REE-enriched fluorite. Therefore, compared to Type 2a fluorite (without sulfides), Type 2b fluorite (with sulfides) has higher REE concentrations (Table 1).

6.2. REE fractionation

REE fractionation in fluids depends on both preferential adsorption of REE on mineral surfaces and preferential complexation of REE with different ligands (Bau, 1991; Bau and Dulski, 1995; Chen and Zhao, 1997; Schönenberger et al., 2008). Generally, preferential REE-adsorption and complexation result in the relative enrichment in LREE and depletion of LREE in fluids (e.g. Bau and Möller, 1992; Schwinn and Markl, 2005). With increasing pH and decreasing temperature, the REE-adsorption decreases and the complexation increases (Ehya, 2012). Hydrothermal mineral paragenesis can also affect the REE patterns of fluorite, because REEs can enter the lattice of minerals such as calcite. Thus, the REE abundance in hydrothermal fluids

depends mainly on the deposition order of the REE-bearing minerals, regardless of the ultimate REE source (e.g. Castorina et al., 2008; Ehya, 2012). At the Tumen deposit, however, the carbonate minerals were generally precipitated later than fluorite, and thus had no effect on the REE content in the fluorite.

All the fluorite samples from the Tumen deposit are relatively enriched in LREE (Table 1; Fig. 5), with $(La/Yb)_N$ ranging from 1.83 to 25.6. LREE-enrichment is characteristic of the fluorite formed under high-temperature (T) and low-pH (Ehya, 2012). The fluorite at Tumen is shown to have deposited from the fluids with high-T (Deng et al., 2013c) and low-pH (see above). The fluorites of Types 1 and 2a have fluid inclusion homogenization temperatures clustering around 360–420 °C and 220–300 °C, respectively (Deng et al., 2013c), and have well-matched $(La/Yb)_N$ averages of 16 ± 6.9 and 5.3 ± 1.8, respectively. The difference in $(La/Yb)_N$ values between the Type 2a and 2b fluorite (Fig. 5) is possibly related to the partition of REE in sulfides coexisting with Type 2b fluorite (Deng, 2011). Nevertheless, Type 2b fluorite samples still show lower $(La/Yb)_N$ values than Type 1 fluorite (Table 1). Nonetheless, the REE patterns and their changes in the various types of fluorite at the Tumen deposit resemble a common scenario where fluorite is deposited in an early hydrothermal stage that is enriched in LREE, whereas later fluorite stage is relatively enriched in HREE (e.g. Ekambaram et al., 1986; Eppinger and Closs, 1990; Hill et al., 2000; Möller et al., 1976).

Möller (1991) linked the LREE-enrichment in fluorites to a high Ca^{2+}/F^- ratio in parent fluids, and Lüders (1991) suggested that fluids with high Ca^{2+}/F^- ratios neither come from an F-rich source nor from a re-mobilized pre-existing fluorite system in deeper parts of the crust. Thus, we prefer to attribute the high Ca^{2+}/F^- ratio of the fluid at Tumen to the carbonate hostrocks, which could provide enough Ca^{2+} for the hydrothermal system during fluid–rock interactions.

6.3. Tb/Ca and Tb/La ratios

Tb/Ca and Tb/La ratios have been used to discriminate fluorite occurrences according to their sedimentary, hydrothermal and pegmatitic affinities (Möller et al., 1976). The composition of various stages of fluorite here studied defines fields and trends using a constant and stoichiometric abundance of Ca in ideal fluorite, as outlined by Möller et al. (1976). Gagnon et al. (2003) proved that a small amount of trace elements incorporated into fluorite does not change the overall discrimination.

Most of the data from this study plot in the hydrothermal field and broadly defines a linear trend from Stage 1 to Stage 2 fluorite on the Tb/Ca versus Tb/La diagram in Fig. 6, except for Type 2b fluorite that has lower Tb/Ca ratio, which possibly results from the coeval precipitation of an unidentified LREE-enriched phase (Chesley et al., 1991). This suggests that the REE was progressively incorporated into the fluorites during hydrothermal precipitation.

6.4. Y–Ho fractionation

The mean Y content of the fluorite samples increases from 4.87 ppm in Type 1, through 14.3 ppm in Type 2a, to 22.8 ppm in Type 2b, with the Y/Y^* ratios increasing from 1.59 ± 0.46 through 1.92 ± 0.35 to 2.18 ± 0.48, respectively (Table 1). The pronounced positive Y anomalies in these fluorite samples are suggestive of strong Y—Ho fractionation in the Tumen hydrothermal system. Möller (1998) linked significant enrichment in Y to the presence of fluoride complexing agents, and Bau (1996) proposed that Y–F complexes are more stable than Ho–F complexes, which can be deduced using the "Hard and Soft Acids and Bases" (HSAB) theory of Pearson (1963), which is a qualitative concept attempting to explain the stability of metal complexes and the mechanisms of their reactions (also see Chen and Fu, 1991; Tang et al., 2013). Therefore, Y preferentially remains in F-rich fluids, and fluorite deposited from fluids has increasing Y contents and Y/Y^* ratios from the early to late mineralisation stages.

Bau and Dulski (1995) proposed that the Y—Ho fractionation is not source-related, but depends on fluid composition and fluid migration, and that hydrothermal fluorites are characterized by variable and non-chondritic Y/Ho ratios of >200 (Fig. 7). The Y/Ho ratios of fluorite samples from the Tumen deposit range from 33 to 71 (Table 1), obviously different from the chondritic Y/Ho ratios of 28 (Anders and Grevesse, 1989), but well overlapped by the Y/Ho ratios of hydrothermal fluorites (Fig. 7). Moreover, they appear to be a mixture of igneous rocks and seawater (Fig. 7), and similar to chemical sediments such as the carbonate rocks within the Guanmenshan Formation in northeastern NCC, whose Y/Ho ratios range from 34.5 to 56.6 (for details see Tang et al., 2013). Therefore, the Y/Ho ratios suggest that the fluorite at the Tumen deposit was formed by the interaction of magmatic fluids with carbonate wallrocks.

The La/Ho ratios of the Type 1 fluorite averages 43.9 ± 20.7, which is much higher than the average of Type 2a (13.1 ± 4.4) fluorite. Conversely, the Y/Ho average for Type 1 fluorite is 44.1 ± 12.6, which is lower than that of Type 2a (50.5 ± 8.7) fluorite. Despite the paucity of data, a negative correlation between the Y/Ho and La/Ho ratios is observed at the Tumen deposit (Fig. 8; Bau and Dulski, 1995). However, two samples of the Type 1 fluorite show a large La/Ho variation, which differs from the Y/Ho values (Fig. 8). This possibly results from the formation of an enriched LREE phase or the partial loss of a LREE-enriched phase during fluorite re-crystallization (Bau and Dulski, 1995). The presence of secondary fluid inclusions in Type 1 fluorite crystals, as observed by Deng et al. (2013c), supports that some of the Type 1 fluorite grains were re-crystallized or modified in late hydrothermal

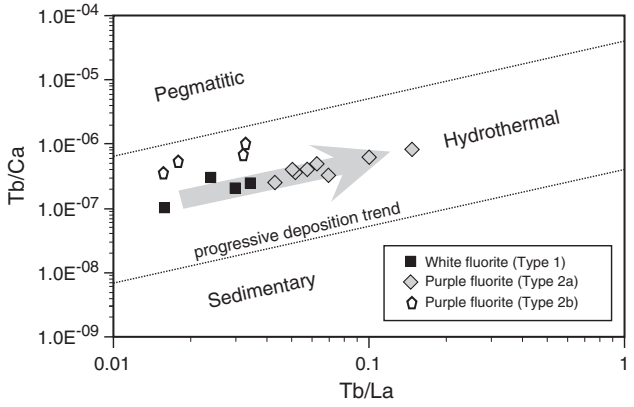

Fig. 6. Plots of Tb/Ca versus Tb/La ratios for fluorite from the Tumen Mo–F deposit. Primary crystallization trend represents degree of differentiation during fluorite crystallization (after Möller et al., 1976).

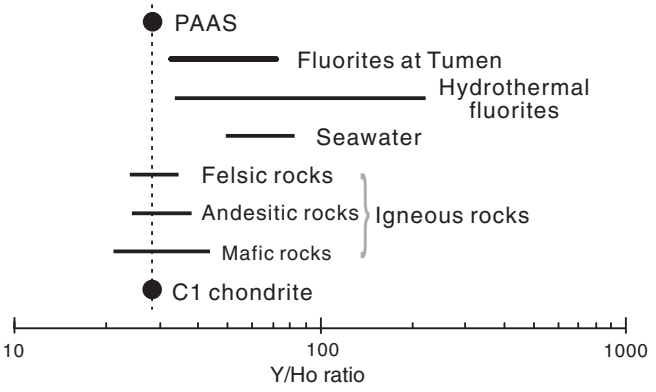

Fig. 7. Comparison of the Y/Ho ratios of fluorite from the Tumen Mo–F deposit with other kinds of geological bodies (after Bau and Dulski, 1995). PAAS stands for the Post-Archaean Australian Shale.

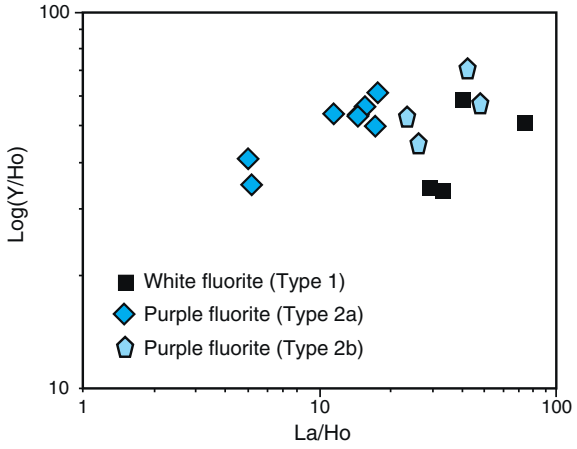

Fig. 8. Plots of Y/Ho versus La/Ho ratios in fluorite from the Tumen deposit.

stages. In addition, the Type 2b fluorite samples have high La/Ho ratios, which may be the result from the coeval precipitation of an unidentified LREE-enriched phase.

6.5. Eu and Ce anomalies

The Eu/Eu* ratio is a useful indicator of the physicochemical features of fluids, including temperature, pH and fO_2 (Bau and Möller, 1992; Chen and Fu, 1991; Möller, 1998; Möller and Holzbecher, 1998). Thermochemical reduction of Eu^{3+} to Eu^{2+} can happen at high temperatures, and hydrothermal fluorite formed above 200 °C usually show Eu-enrichment relative to the fluids (Schwinn and Markl, 2005). During REE leaching from rocks, Eu^{2+} accumulates at high-T or reducing fluids, resulting in a positive Eu anomaly in fluids and a negative one in leached rocks (Castorina et al., 2008; Chen and Zhao, 1997).

The Eu/Eu* ratios decrease from 1.11 ± 0.35 in Type 1, through 0.89 ± 0.19 in Type 2a, to 0.75 ± 0.17 in Type 2b fluorites at the Tumen deposit (Table 1), generally with no to weak positive or negative Eu anomalies (Fig. 5). This suggests that the fluorite precipitated from fluids with decreasing temperature or increasing fO_2 (Chen and Zhao, 1997; Schwinn and Markl, 2005). Alternatively, some other Eu-depleted minerals co-precipitated with the Type 1 fluorite, whilst Eu-enriched minerals co-precipitated with the Type 2b fluorite. As mentioned above, the decrease in Eu/Eu* values from Type 1 to Type 2a fluorites can be interpreted by considering any one or a combination of factors such as an increase in pH, increase in fO_2, and decrease in temperature. However, this does not explain the Eu/Eu* difference between Type 2a and Type 2b fluorites, because both types were formed during Stage 2. As known earlier, Type 2b fluorite coexists with sulfides that are generally characterized by low ΣREE values and positive Eu-anomalies (Tang et al., 2013 and references therein), which explains why Type 2b fluorite has lower Eu/Eu* values compared to Type 2a fluorite. In addition, the Eu-enrichment of Stage 1 fluorite would have lead to a relative Eu-depletion in the mineralising fluids from which Stage 2 fluorite was deposited and characterized by lower Eu/Eu* values.

The Ce/Ce* ratio is another indicator of the physicochemical features of fluids. The slightly negative Ce anomalies in Stage 2 fluorites indicate that the parent fluid was somewhat reducing (Möller, 1998). This is consistent with the positive Eu anomalies in Stage 1 fluorite and the presence of sulfides at the deposit. Alternatively, the negative Ce anomalies could have been inherited from the parent fluid (Castorina et al., 2008; Ehya, 2012), but this hypothesis is not supported by the Stage 1 fluorite, which are not depleted in Ce.

The negative Ce anomaly may also be related to hydroxide complexation (Schönenberger et al., 2008). The hydroxide complex with Ce is more stable than those with other REE (Haas et al., 1995), which leads Ce to remain in a fluid and, consequently, a negative Ce anomaly can be expected in the precipitants.

6.6. Source of REE and fluids

Considering the fluid–rock interaction and the similarity in the REE patterns of the fluorites and the hostrocks assigned to the Luanchuan Group (Table 2; Fig. 9a), we propose that the hostrocks are a major source for the REE concentration at the Tumen deposit. The hostrocks have broadly similar REE patterns in each orebody at the deposit. The low REE concentrations in fluorite at the deposit support the hypothesis that the REE source is the marine limestone units within the Luanchuan Group.

Although the Tumen deposit is in a close vicinity to intrusive rocks (Fig. 1d) and genetically related to the intrusive rocks, the REE patterns of the fluorite samples from the deposit are notably different from those of the igneous rocks (Table 2), including the Early and Late Yanshanian granites (Fig. 9b, c), Neoproterozoic monzogranite and syenite (Fig. 9d, f), as well as the volcanic rocks in the Xiong'er Group (Fig. 9e). This indicates that the fluorites are not necessarily related to these igneous rocks. However, as shown in Table 2, the LREE/HREE and $(La/Nd)_N$ ratios in Stage 1 fluorite are higher than those in the Luanchuan Group, but lower than those of the nearby Neoproterozoic syenite. This suggests that the Neoproterozoic syenite is a possibly complementary source for REE during the early stages of the Tumen hydrothermal system (Fig. 9f). Moreover, experimental studies by Wendlandt and Harrison (1979) have shown that LREE-enriched fluids could be sourced from highly evolved syenites. Therefore, we suggest that in addition to the hostrocks in the Luanchuan Group, the Neoproterozoic syenitic magma could have been associated with fluids and is a source for REE contributing to the development of the Tumen deposit. This interpretation is strongly supported by: (1) the zircon U–Pb age of 844 ± 2 Ma for the Shuangshan Syenite (Bao et al., 2008), which is the same within error to the molybdenite Re–Os isochron age of 847 ± 7 Ma (Deng et al., 2013c); (2) the fluid inclusion types and microthermometric results are comparable with typical magmatic hydrothermal mineral

Table 2
REE geochemical signatures of fluorite at Tumen deposit and regional rocks (ppm).

Rock/mineral	Type 1 fluorite	Type 2a fluorite	Type 2b fluorite	Neo-Pt Luanchuan Group	Neo-Pt syenite dyke	Neo-Pt biotite monzogranite	Meso-Pt Xiong'er Group	Early Yanshanian granite	Late Yanshanian granite
ΣREE	20.7	23.0	55.2	152	883	83.0	314	37.7	62.0
LREE	18.7	18.1	48.3	135	840	72.5	283	35.4	60.3
HREE	2.00	4.90	6.90	17.7	43.3	10.5	31.5	2.35	1.70
LREE/HREE	9.80	4.00	7.50	7.62	19.4	6.92	9.00	15.1	32.0
Tb/La	0.03	0.03	0.02	0.03	0.01	0.02	0.03	0.01	0.01
Y/Ho	41.9	47.7	54.3		30.2	23.8	25.3	19.4	30.4
$(La/Nd)_N$	2.4	1.5	3.2	2.11	3.25	2.36	2.01	5.89	3.30
$(Gd/Yb)_N$	2.9	2.4	2.0	1.56	2.39	1.56	1.56	1.96	3.62
Eu/Eu*	1.11	0.89	0.75	0.62	0.40	0.64	0.73	0.87	0.73
Ce/Ce*	0.96	0.86	0.84	0.88	0.92	0.87	1.03	0.74	1.13
Y/Y*	1.59	1.92	2.18		1.14	0.92	0.98	0.90	1.16

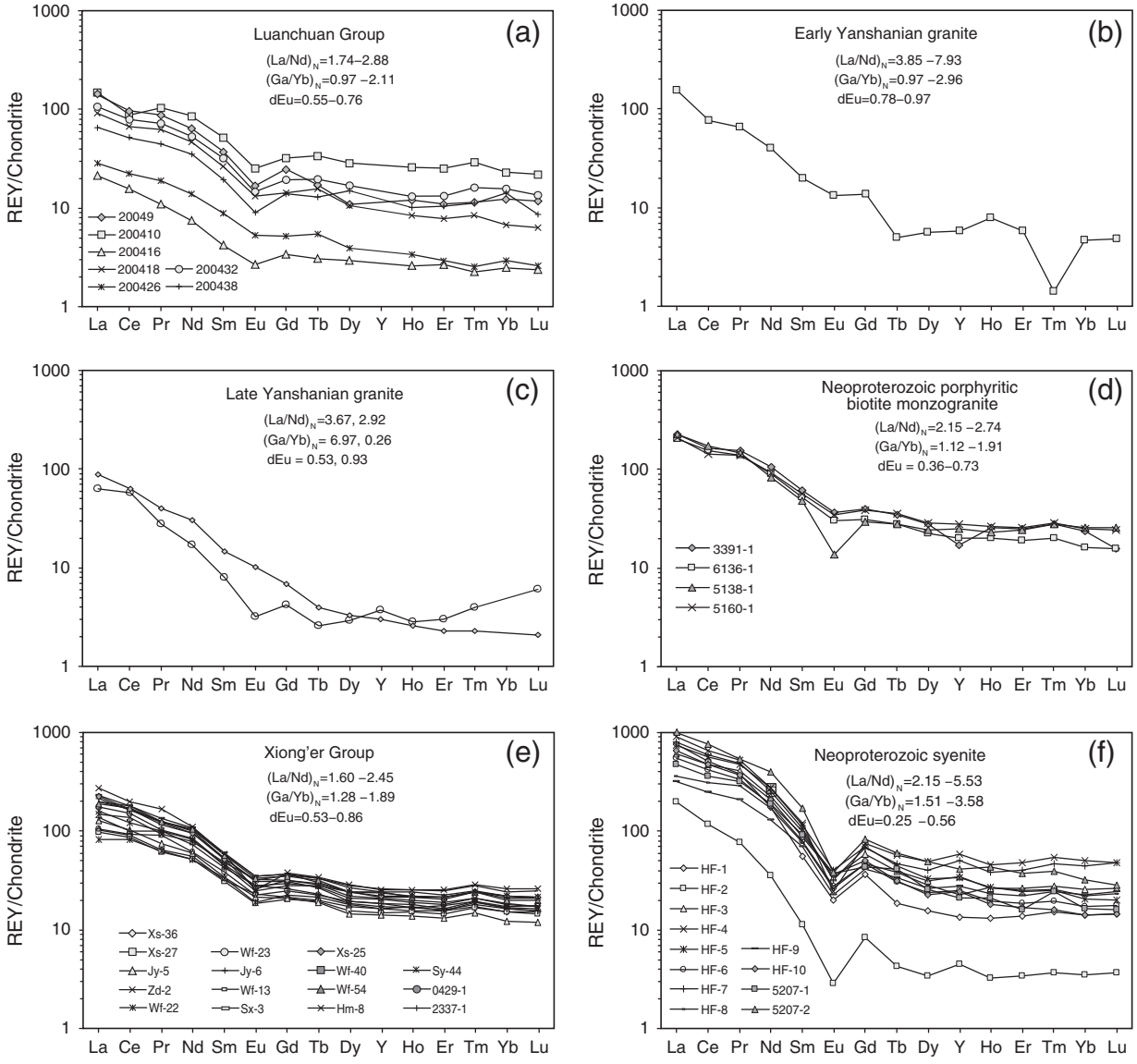

Fig. 9. REE distribution patterns of the geological bodies in or close to the Tumen deposit. Data sources: Luanchuan Group from Xing (2005); Xiong'er Group from T.P. Zhao et al. (2002); the syenite from Bao et al. (2008); and the others from GMRBHP (1989).

systems (Deng et al., 2013c); and (3) oxygen–hydrogen isotope data show that the ore-forming fluids were initially magmatic in source, and then progressively added to by an evolved to meteoric water (Deng et al., 2013c).

7. Conclusions

The Tumen Mo–F deposit in the southern margin of the NCC is hosted by dolostone assigned to the Neoproterozoic Luanchuan Group. The deposit consists of veins predominantly composed of fluorite, calcite, molybdenite and pyrite. Hydrothermal mineralisation in the area includes four stages progressing from veins of white fluorite in the early stage, through purple fluorite(–molybdenite–pyrite) and sulfide–calcite, to carbonate at the last stage.

The ΣREE content in the fluorite is low, but increases from Stage 1 to Stage 2, which is related to increasing pH and a chemically reducing fluid. From Stage 1 to Stage 2, the Eu/Eu*, Ce/Ce* and $(La/Yb)_N$ ratios in the fluorite decreases, but the Y/Y* ratio increases, which coincidently suggest that the fluid became less reducing, less acidic and lower in temperature.

The Tb/Ca and Tb/La ratios in the fluorite studied confirm that the REE were progressively incorporated into the fluorites during hydrothermal mineralisation. The Y/Ho ratios are typical of hydrothermal fluorites that were likely formed by the interaction of magmatic fluids with the carbonate wallrocks.

The REE in the fluorite is predominantly sourced from carbonate-dominated hostrocks assigned to the Luanchuan Group, although the fluids were initially associated with Neoproterozoic syenite in the region. The tectonic setting and genesis of the mineralisation in the East Qinling Mo Belt during ca. 850 Ma is summarised in Fig. 10 (modified after Chen and Fu, 1992).

Acknowledgements

The research was supported by the 973-Project (Nos. 2012CB416602, 2006CB403508), the National Natural Science Foundation of China (Nos. 41202050, 41072061) and China Postdoctoral Science Foundation (No. 2012M510261). This contribution is partly from the Australian Research Council (ARC) Centre of Excellence for Core to Crust Fluid Systems (http://www.ccfs.mq.edu.au), which one of us (L. Bagas) is associated with. Dr. Zhen-Lei Yuan helped during the field investigation,

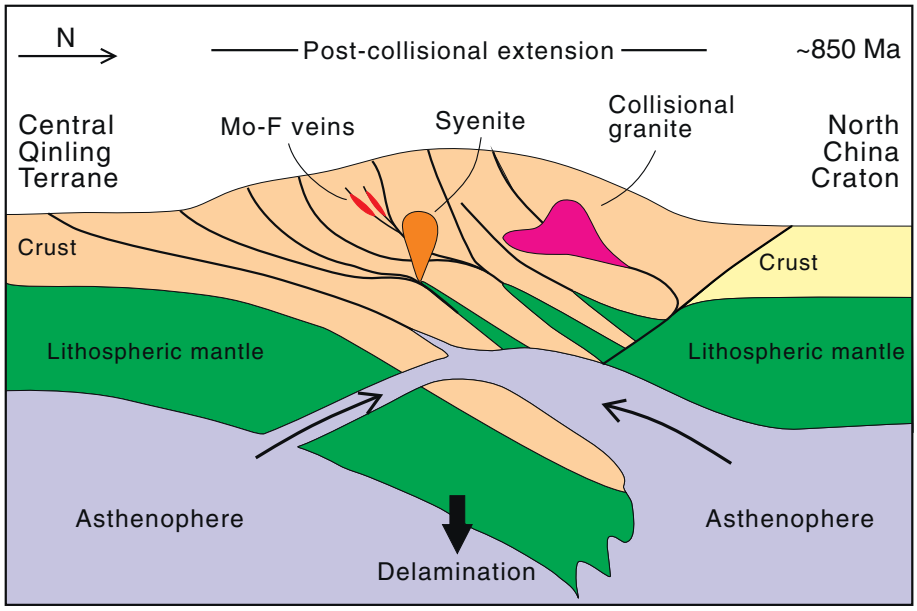

Fig. 10. Sketch illustrating the proposed tectonic setting of the East Qinling Mo Belt during ca. 850 Ma (modified after Chen and Fu, 1992).

and Dr. Xin-Di Jin helped with the trace element analyses. Corrections, comments and suggestions from two reviewers and Professor Cheng Xu greatly improved the quality of the paper.

References

Anders, E., Grevesse, N., 1989. Abundances of the elements: meteoritic and solar. Geochim. Cosmochim. Acta 53, 197–214.
Bao, Z.W., Wang, Q., Bai, G.D., Zhao, Z.H., Song, Y.W., Liu, X.M., 2008. Geochronology and geochemistry of the Fangcheng Neoproterozoic alkali-syenites in East Qinling orogen and its geodynamic implications. Chin. Sci. Bull. 53, 2050–2061.
Bau, M., 1991. Rare-earth element mobility during hydrothermal and metamorphic fluid rock interaction and the significance of the oxidation-state of Europium. Chem. Geol. 93, 219–230.
Bau, M., 1996. Controls on the fractionation of isovalent trace elements in magmatic and aqueous systems: evidence from Y/Ho, Zr/Hf, and lanthanide tetrad effect. Contrib. Mineral. Petrol. 123, 323–333.
Bau, M., Dulski, P., 1995. Comparative study of yttrium and rare-earth element behaviours in fluorine-rich hydrothermal fluids. Contrib. Mineral. Petrol. 119, 213–223.
Bau, M., Dulski, P., 1996. Distribution of yttrium and rare-earth elements in the Penge and Kuruman iron-formations, Transvaal Supergroup, South Africa. Precambrian Res. 79, 37–55.
Bau, M., Möller, P., 1992. Rare-earth element fractionation in metamorphogenic hydrothermal calcite, magnesite and siderite. Miner. Petrol. 45, 231–246.
Bau, M., Romer, R.L., Lüders, V., Dulski, P., 2003. Tracing element sources of hydrothermal mineral deposits: REE and Y distribution and Sr–Nd–Pb isotopes in fluorite from MVT deposits in the Pennine Orefield, England. Miner. Deposita 38, 992–1008.
Bureau of geology and mineral resources of Hanan Province, 1989. Regional Geology of Henan Province. Geological Publishing House, Beijing (772 pp. (in Chinese)).
Cao, J.C., 1997. Geochemistry of REE of fluorite deposits and physical properties of fluorite mineral in China. Geol. Process. 33, 18–23 (in Chinese with English abstract).
Castorina, F., Masi, U., Padalino, G., Palomba, M., 2008. Trace-element and Sr–Nd isotopic evidence for the origin of the Sardinian fluorite mineralization (Italy). Appl. Geochem. 23, 2906–2921.
Chen, Y.J., 2013. The development of continental collision metallogeny and its application. Acta Petrol. Sin. 29, 1–17 (in Chinese with English abstract).
Chen, Y.J., Fu, S.G., 1991. Variation of REE patterns in early Precambrian sediments: theoretical study and evidence from the southern margin of the northern China craton. Chin. Sci. Bull. 36, 1100–1104.
Chen, Y.J., Fu, S.G., 1992. Gold Mineralization in West Henan, China. Chinese Seismological Press, Beijing (234 pp. (in Chinese with English abstract)).
Chen, Y.J., Li, N., 2009. Nature of ore-fluids of intracontinental intrusion-related hypothermal deposits and its difference from those in island arcs. Acta Petrol. Sin. 25, 2477–2508.
Chen, Y.J., Zhao, Y.C., 1997. Geochemical characteristics and evolution of REE in the Early Precambrian sediments: evidences from the southern margin of the North China craton. Episodes 20, 109–116.
Chen, Y.J., Li, C., Zhang, J., Li, Z., Wang, H.H., 2000. Sr and O isotopic characteristics of porphyries in the Qinling molybdenum deposit belt and their implication to genetic mechanism and type. Sci. China Ser. D 43, 82–94.
Chen, Y.J., Chen, H.Y., Zaw, K., Pirajno, F., Zhang, Z.J., 2007. Geodynamic settings and tectonic model of skarn gold deposits in China: an overview. Ore Geol. Rev. 31, 139–169.
Chen, Y.J., Zhai, M.G., Jiang, S.Y., 2009. Significant achievements and open issues in study of orogenesis and metallogenesis surrounding the North China continent. Acta Petrol. Sin. 25, 2695–2726 (in Chinese with English abstract).
Chesley, J.T., Halliday, A.N., Scrivener, R.C., 1991. Samarium–neodymium direct dating of fluorite mineralization. Science 252, 949–951.
Dai, A.B., 1987. Coordination Chemistry. Science Press, Beijing (870 pp. (in Chinese)).
Deng, X.H., 2011. Anatomy and Comparative Study on the Multiple Molybdenum Mineralization Pulses in East Qinling Orogenic Belt. Ph.D. Thesis Peking University, Beijing (239 pp. (in Chinese with English abstract)).
Deng, X.H., Li, W.B., Li, N., Mei, M., Zhang, Y., 2008. Fluid inclusion constraints on the origin of Zhifang Mo deposit Songxian county, Henan provine. Acta Petrol. Sin. 24, 2133–2148 (in Chinese with English abstract).
Deng, X.H., Chen, Y.J., Santosh, M., Yao, J.M., 2013a. Genesis of the 1.76 Ga Zhaiwa Mo–Cu and its link with the Xiong'er volcanics in the North China Craton: implications for accretionary growth along the margin of the Columbia supercontinent. Precambrian Res. 227, 337–348.
Deng, X.H., Chen, Y.J., Santosh, M., Zhao, G.C., Yao, J.M., 2013b. Metallogeny during continental outgrowth in the Columbia supercontinent: isotopic characterization of the Zhaiwa Mo–Cu system in the North China Craton. Ore Geol. Rev. 51, 43–56.
Deng, X.H., Chen, Y.J., Santosh, M., Yao, J.M., 2013c. Re–Os geochronology, fluid inclusions and genesis of the 0.85 Ga Tumen molybdenite–fluorite deposit in Eastern Qinling, China: implications for pre-Mesozoic Mo-enrichment and tectonic setting. Geol. J. 48, 484–497.
Dong, Y.P., Zhang, G.W., Neubauer, F., Liu, X.M., Genser, J., Hauzenberger, C., 2011. Tectonic evolution of the Qinling orogen, China: review and synthesis. J. Asian Earth Sci. 41, 213–237.
Ehya, F., 2012. Variation of mineralizing fluids and fractionation of REE during the emplacement of the vein-type fluorite deposit at Bozijan, Markazi Province, Iran. J. Geochem. Explor. 112, 93–106.
Ekambaram, V., Brookins, D.G., Rosenberg, P.E., Emanuel, K.M., 1986. REE geochemistry of fluorite–carbonate deposits in Western Montana, USA. Chem. Geol. 54, 319–331.
Eppinger, R.G., Closs, L.G., 1990. Variation of trace elements and rare earth elements in fluorite: a possible tool for exploration. Econ. Geol. Bull. Soc. 85, 1896–1907.
Gagnon, J.E., Samson, I.M., Fryer, B.J., Williams-Jones, A.E., 2003. Compositional heterogeneity in fluorite and the genesis of fluorite deposits: insights from LA-ICP-MS analysis. Can. Mineral. 41, 365–382.
Goff, B.H., Weinberg, R., Groves, D.I., Vielreicher, N.M., Fourie, P.J., 2004. The giant Vergenoeg fluorite deposit in a magnetite–fluorite–fayalite REE pipe: a hydrothermally-altered carbonatite-related pegmatoid? Miner. Petrol. 80, 173–199.
Gramaccioli, C.M., Diella, V., Demartin, F., 1999. The role of fluoride complexes in REE geochemistry and the importance of *4f* electrons: some examples in minerals. Eur. J. Mineral. 11, 983–992.
Haas, J.R., Shock, E.L., Sassani, D.C., 1995. Rare earth in hydrothermal systems: estimates of standard partial molal thermodynam ic of aqueous complexes of rare earth elements at high pressures and temperatures. Geochim. Cosmochim. Acta 59, 4329–4350.
He, Y.H., Zhao, G.C., Sun, M., Xia, X.P., 2009. SHRIMP and LA-ICP-MS zircon geochronology of the Xiong'er volcanic rocks: Implications for the Paleo-Mesoproterozoic evolution of the southern margin of the North China Craton. Precambrian Res. 168, 213–222.
Hill, G.T., Campbell, A.R., Kyle, P.R., 2000. Geochemistry of southwestern New Mexico fluorite occurrences implications for precious metals exploration in fluorite-bearing systems. J. Geochem. Explor. 68, 1–20.
Hu, S.X., 1988. Geology and Metallogeny of the Collision Belt Between the North and the South China Plates. Nanjing University Press, Nanjing (558 pp. (in Chinese)).

Jiang, G.Q., Zhou, H.R., Wang, Z.Q., 1994. Stratigraphic sequence, sedimentary environment and its tectono-paleogeographic significance of the Luanchuan Group, Luanchuan area, Henan Province. Geoscience 8, 430–440 (in Chinese with English abstract).
Jiang, Y.H., Ling, H.F., Jiang, S.Y., Shen, W.Z., Fan, H.H., Ni, P., 2006. Trace element and Sr–Nd isotope geochemistry of fluorite from the Xiangshan uranium deposit south-east China. Econ. Geol. 101, 1613–1622.
Jin, X.D., Zhu, H.P., 2000. Determination of 43 trace elements in rock samples by double focusing high resolution inductively coupled plasma-mass spectrometry. Chin. J. Anal. Chem. 28, 563–567 (in Chinese with English abstract).
Li, N., Chen, Y.J., Zhang, H., Zhao, T.P., Deng, X.H., Wang, Y., Ni, Z.Y., 2007. Molybdenum deposits in East Qinling. Earth Sci. Front. 14, 186–198 (in Chinese with English abstract).
Li, N., Chen, Y.J., Fletcher, I.R., Zeng, Q.T., 2011a. Triassic mineralization with Cretaceous overprint in the Dahu Au–Mo deposit, Xiaoqinling gold province: constraints from SHRIMP monazite U–Th–Pb geochronology. Gondwana Res. 20, 543–552.
Li, N., Chen, Y.J., Santosh, M., Yao, J.M., Sun, Y.L., Li, J., 2011b. The 1.85 Ga Mo mineralization in the Xiong'er Terrane, China: implications for metallogeny associated with assembly of the Columbia supercontinent. Precambrian Res. 186, 220–232.
Li, N., Chen, Y.J., Pirajno, F., Gong, H.J., Mao, S.D., Ni, Z.Y., 2012a. LA-ICP-MS zircon U–Pb dating, trace element and Hf isotope geochemistry of the Heyu granite batholith, eastern Qinling, central China: implications for Mesozoic tectono-magmatic evolution. Lithos 142–143, 34–47.
Li, N., Ulrich, T., Chen, Y.J., Thompson, T.B., Peace, V., Pirajno, F., 2012b. Fluid evolution of the Yuchiling porphyry Mo deposit, East Qinling, China. Ore Geol. Rev. 48, 442–459.
Li, N., Chen, Y.J., Pirajno, F., Ni, Z.Y., Sun, Y.L., 2013. Timing of the Yuchiling giant porphyry Mo system, eastern Qinling, central China, and implications for ore genesis. Miner. Deposita 48, 505–524.
Lüders, V., 1991. Formation of hydrothermal fluorite deposits of the Harz Mountains, Germany. In: Pagel, M., Leroy, J.L. (Eds.), Source. Transport and Deposition of Metals. Balkema, Rotterdam, pp. 325–328.
Mao, J.W., Xie, G.Q., Bierlein, F., Qu, W.J., Du, A.D., Ye, H.S., Pirajno, F., Li, H.M., Guo, B.J., Li, Y.F., Yang, Z.Q., 2008. Tectonic implications from Re–Os dating of Mesozoic molybdenum deposits in the East Qinling–Dabie orogenic belt. Geochim. Cosmochim. Acta 72, 4607–4626.
Mcdonough, W.F., Sun, S.S., 1995. The composition of the Earth. Chem. Geol. 120, 223–253.
Michard, A., 1989. Rare earth element systematics in hydrothermal fluids. Geochim. Cosmochim. Acta 53, 745–750.
Möller, P., 1991. REE fractionation in hydrothermal fluorite and calcite. In: Pagel, M., Leroy, J. (Eds.), Source, Transport and Deposition of Metals. Balkema, Rotterdam, pp. 91–94.
Möller, P., 1998. Europium Anomalies in Hydrothermal Minerals. Kinetic Versus Thermodynamic Interpretation. Proceedings of the Ninth Quadrennial IAGOD Symposium Schweizerbart, Stuttgart, pp. 239–246.
Möller, P., 2001. The behaviour of REE and Y in water–rock interactions. Water Rock Interact. 1–2, 989–992.
Möller, P., Holzbecher, E., 1998. Eu anomalies in hydrothermal fluids and minerals. A combined thermochemical and dynamic phenomenon. Freib. Forsch. 475, 73–84.
Möller, P., Parekh, P., Schneider, J., 1976. The application of Tb/Ca–Tb/La abundance ratios to problems of fluorspar genesis. Miner. Deposita 11, 111–116.
Pearson, R.G., 1963. Hard and soft acids and bases. J. Am. Chem. Soc. 85 (22), 3533–3539.
Peng, P., Zhai, M.G., Ernst, R.E., Guo, J.H., Liu, F., Hu, B., 2008. A 1.78 Ga large igneous province in the North China craton: the Xiong'er volcanic province and the North China dyke swarm. Lithos 101, 260–280.
Phillips, G.N., Evans, K.A., 2004. The role of CO_2 in the formation of gold deposits. Nature 429, 860–863.
Pirajno, F., 2009. Hydrothermal Processes and Mineral Systems. Springer, Berlin (1250 pp.).
Pirajno, F., 2013. The Geology and Tectonics Settings of China's Mineral Deposits. Springer, Berlin (679 pp.).
Ratschbacher, L., Hacker, B.R., Calvert, A., Webb, L.E., Grimmer, J.C., McWilliams, M.O., Ireland, T., Dong, S.W., Hu, J.M., 2003. Tectonics of the Qinling (Central China): tectonostratigraphy, geochronology, and deformation history. Tectonophysics 366, 1–53.
Ronchi, L.H., Touray, J.C., Michard, A., Dardenne, M.A., 1993. The ribeira fluorite district, southern Brazil: geological and geochemical (REE, Sm–Nd isotopes) characteristics. Miner. Deposita 28, 240–252.
Sánchez, V., Cardellach, E., Corbella, M., Vindel, E., Martín-Crespo, T., Boyce, A.J., 2010. Variability in fluid sources in the fluorite deposits from Asturias (N Spain): further evidences from REE, radiogenic (Sr, Sm, Nd) and stable (S, C, O) isotope data. Ore Geol. Rev. 37, 87–100.
Santosh, M., 2010. Assembling North China Craton within the Columbia supercontinent: the role of double-sided subduction. Precambrian Res. 178, 149–167.
Santosh, M., Tsunogae, T., Li, J.H., Liu, S.J., 2007a. Discovery of sapphirine-bearing Mg–Al granulites in the North China Craton: implications for paleoproterozoic ultrahigh temperature metamorphism. Gondwana Res. 11, 263–285.
Santosh, M., Wilde, S.A., Li, J.H., 2007b. Timing of Paleoproterozoic ultrahigh-temperature metamorphism in the North China Craton: evidence from SHRIMP U–Pb zircon geochronology. Precambrian Res. 159, 178–196.
Schönenberger, J., Köhler, J., Markl, G., 2008. REE systematics of fluorides, calcite and siderite in peralkaline plutonic rocks from the Gardar Province, South Greenland. Chem. Geol. 247, 16–35.
Schwinn, G., Markl, G., 2005. REE systematics in hydrothermal fluorite. Chem. Geol. 216, 225–248.
Subías, I., Fernández-Nieto, C., 1995. Hydrothermal events in the valle-de-tena (Spanish western pyrenees) as evidenced by fluid inclusions and trace element distribution from fluorite deposits. Chem. Geol. 124, 267–282.
Sun, S., Zhang, G.W., Chen, Z.M., 1985. Geologic Evolution of the South of the North China Fault-block. China Metallurgical Industry Press, Beijing (267 pp. (in Chinese)).
Tang, H.S., Chen, Y.J., Wu, G., Yang, T., 2009. Rare earth element geochemistry of carbonates of Dashiqiao Formation, Liaohe Group, eastern Liaoning province: implications for Lomagundi event. Acta Petrol. Sin. 25, 3075–3093 (in Chinese with English abstract).
Tang, H.S., Chen, Y.J., Santosh, M., Zhong, H., Yang, T., 2013. REE geochemistry of carbonates from the Guanmenshan Formation, Liaohe Group, NE Sino-Korean Craton: implications for seawater compositional change during the Great Oxidation Event. Precambrian Res. 227, 316–336.
Taylor, S.R., McLennan, S.M., 1985. The Continental Crust: Its Composition and Evolution. Blackwell, Oxford (312 pp.).
Wan, Y., Wilde, S.A., Liu, D.Y., Yang, C.X., Song, B., Yin, X.Y., 2006. Further evidence for 1.85 Ga metamorphism in the Central Zone of the North China Craton: SHRIMP U–Pb dating of zircon from metamorphic rocks in the Lushan area, Henan Province. Gondwana Res. 9, 189–197.
Wang, X.L., Jiang, S.Y., Dai, B.Z., Griffin, W.L., Dai, M.N., Yang, Y.H., 2011. Age, geochemistry and tectonic setting of the Neoproterozoic (ca. 830 Ma) gabbros on the southern margin of the North China Craton. Precambrian Res. 190, 35–47.
Wen, T.X., 1997. The geological characteristics of fluorite ore belts in Fangcheng. Henan Geol. 15, 103–107 (in Chinese).
Wendlandt, R.F., Harrison, W.J., 1979. Rare-earth partitioning between immiscible carbonate and silicate liquids and CO_2 vapor-results and implications for the formation of light rare earth-enriched rocks. Contrib. Mineral. Petr. 69, 409–419.
Xing, K., 2005. Study on the Stratigraphic Characters of the Luanchuan Group and the Ralation to Pb–Zn Deposit Mineralization in the Southwest of Henan Province. China Universtiy of Geosciences, Beijing (Master Degree Thesis, 77 pp. (in Chinese with English abstract)).
Xu, X.S., Griffin, W.L., Ma, X., O'Reilly, S.Y., He, Z.Y., Zhang, C.L., 2009. The Taihua group on the southern margin of the North China craton: further insights from U–Pb ages and Hf isotope compositions of zircons. Miner. Petrol. 97, 43–59.
Xu, C., Kynicky, J., Chakhmouradian, A.R., Qi, L., Song, W.L., 2010. A unique Mo deposit associated with carbonatites in the Qinling orogenic belt, central China. Lithos 118, 50–60.
Yang, Y.F., Li, N., Chen, Y.J., 2012. Fluid inclusion study of the Nannihu giant porphyry Mo–W deposit, Henan Province, China: implications for the nature of porphyry ore-fluid systems formed in continental collision regime. Ore Geol. Rev. 46, 83–94.
Yang, Y., Chen, Y.J., Zhang, J., Zhang, C., 2013a. Ore geology, fluid inclusions and four-stage hydrothermal mineralization of the Shangfanggou giant Mo–Fe deposit in Eastern Qinling, central China. Ore Geol. Rev. 55, 146–161.
Yang, Y.F., Chen, Y.J., Li, N., Mi, M., Xu, Y.L., Li, F.L., Wan, S.Q., 2013b. Fluid inclusion and isotope geochemistry of the Qian'echong giant porphyry Mo deposit, Dabie Shan, China: a case of NaCl-poor, CO_2-rich fluid systems. J. Geochem. Explor. 124, 1–13.
Ye, H.N., Li, H.Q., Wang, W.Z., Luo, M.Q., 2004. Molybdenum geochemical features and exploration prospecting from ineral deposits in Tumen of Fangcheng county, Henan province. Miner. Resour. Geol. 18, 260–263 (in Chinese with English abstract).
Zhai, M.G., Santosh, M., 2011. The early Precambrian odyssey of the North China Craton: a synoptic overview. Gondwana Res. 20, 6–25.
Zhao, Z.H., 1997. Geochemical Principle of Trace Element. Science Press, Beijing (238 pp. (in Chinese)).
Zhao, G.C., Cawood, P.A., Wilde, S.A., Sun, M., 2002a. Review of global 2.1–1.8 Ga orogens: implications for a pre-Rodinia supercontinent. Earth-Sci. Rev. 59, 125–162.
Zhao, T.P., Zhou, M.F., Zhai, M.G., Xia, B., 2002b. Paleoproterozoic rift-related volcanism of the Xiong'er Group, North China craton: implications for the breakup of Columbia. Int. Geol. Rev. 44, 336–351.
Zhao, G.C., Sun, M., Wilde, S.A., Li, S.Z., 2004. A Paleo-Mesoproterozoic supercontinent: assembly, growth and breakup. Earth-Sci. Rev. 67, 91–123.
Zhao, G.C., He, Y.H., Sun, M., 2009. The Xiong'er volcanic belt at the southern margin of the North China Craton: petrographic and geochemical evidence for its outboard position in the Paleo-Mesoproterozoic Columbia Supercontinent. Gondwana Res. 16, 170–181.